HHS Public Access

Author manuscript

Nat Nanotechnol. Author manuscript; available in PMC 2014 September 01.

Published in final edited form as:

Nat Nanotechnol. 2014 March ; 9(3): 233–239. doi:10.1038/nnano.2013.302.

Semiconducting Polymer Nanoparticles as Photoacoustic Molecular Imaging Probes in Living Mice

Kanyi Pu[†,‖], **Adam J. Shuhendler**[†,‖], **Jesse V. Jokerst**[†], **Jianguo Mei**[§], **Sanjiv S. Gambhir**[†,‡], **Zhenan Bao**[§], and **Jianghong Rao**[†,*]

[†]Molecular Imaging Program at Stanford, Department of Radiology, School of Medicine, Stanford University, Stanford, California, USA

[‡]Department of Bioengineering and Department of Materials Science & Engineering, Stanford University, Stanford, California, USA

[§]Department of Chemical Engineering, Stanford University, Stanford, California, USA

Abstract

Photoacoustic (PA) imaging holds great promise for the visualization of physiology and pathology at the molecular level with deep tissue penetration and fine spatial resolution. To fully utilize this potential, PA molecular imaging probes have to be developed. Herein we introduce near infrared (NIR) light absorbing semiconducting polymer nanoparticles (SPNs) as a new class of contrast agents for PA molecular imaging. SPNs can produce stronger signal than commonly used single-wall carbon nanotubes and gold nanorods on a per mass basis, permitting whole-body lymph node PA mapping in living mice at a low systematic injection mass. Furthermore, SPNs possess high structural flexibility, narrow PA spectral profiles, and strong resistance to photodegradation and oxidation, which enables development of the first NIR ratiometric PA probe for *in vivo* real-time imaging of reactive oxygen species—vital chemical mediators of many diseases. These results demonstrate SPNs an ideal nanoplatform for developing PA molecular probes.

Introduction

Semiconducting π-conjugated polymers (SPs) are optically and electronically active materials with many applications ranging from electronic devices[1,2] and sensors,[3,4] to tissue engineering.[5] Recently, SPs have been transformed into nanoparticles as a new class of

*jrao@stanford.edu.

‖Both authors contributed equally to this work.

Contributions: K.P., A.J.S. and J.R. conceived of the experiments, K.P. synthesized and characterized the nanoparticles, K.P. and A.J.S. performed *in vitro* and *in vivo* experiments, K.P., A.J.S. and J.R. performed data analysis and wrote the manuscript, J.J. and S.S.G. provided GNR, SWNT, and technical assistance with PA imaging, J.M. and Z.B. synthesized and provided SP2.

Additional information: Supplementary information accompanies this paper at www.nature.com/naturenanotechnology. Reprints and permission information is available online at http://npg.nature.com/reprintsandpermissions/. Correspondence and requests for materials should be addressed to J.R.

Competing financial interests: Dr. Gambhir serves on the board of Endra Inc. and serves as a consultant for Visualsonics Inc., both manufacturers of small animal PA imaging equipment.

photostable fluorescent nanomaterials.[6] These materials are bright, completely organic and absent from heavy metal ion-induced toxicity to living organisms,[7] and thus have been applied for *in vivo* fluorescence (FL) imaging.[6,8,9] However, FL imaging suffers from the general limitations of whole-body optical imaging techniques such as poor spatial resolution and shallow tissue penetration. In comparison, photoacoustic (PA) imaging allows imaging beyond the optical diffusion limit by integrating optical excitation with ultrasonic detection based on the PA effect, providing deeper tissue imaging penetration and higher spatial resolution.[9,10,11] Herein we report that near-infrared (NIR) light absorbing semiconducting polymer nanoparticles (SPNs) can serve as an efficient and stable nanoplatform to allow photons to be used to generate ultrasound (US) waves, permitting *in vivo* PA molecular imaging.

While endogenous molecules (i.e. hemoglobin, melanin) can generate PA contrast, many physiological and pathological processes often elicit little variation in these intrinsic PA signals, and thus it is essential to develop exogenous contrast agents for PA imaging in living subjects.[12] Many materials have been applied as effective PA contrast agents, including small-molecule dyes, metallic nanoparticles, carbon nanotubes and porphysomes.[13–18] For most, signal production mechanism relies on simple accumulation through passive (such as the enhanced permeability and retention effect) or active (binding to a receptor on the cell surface) targeting to sites of interest.[10,12,14–17,19] In contrast, activatable molecular imaging probes can undergo an intrinsic signal evolution upon detecting molecular targets or events, providing a real-time correlation between probe states (i.e. activated *vs.* non-activated) and pathological processes on a molecular level.[20,21] Activatable probes have been developed for other imaging modalities such as FL imaging, and widely used in biology and medicine.[21–23] However, very few NIR activatable probes have been reported for *in vivo* PA molecular imaging except for a very recent example demonstrating imaging of matrix metalloproteinase activity in thyroid tumor xenografts.[24–26] The full utilization of the potential of PA imaging at a depth and spatial resolution that is unattainable by FL imaging requires new materials amenable to the construction of activatable PA probes.

As SPs typically used for solar cells were designed to have high NIR absorption, we evaluated these photovoltaic SPs as building blocks for the development of PA molecular imaging nanoprobes. We found that, depending on the molecular structure of SPs, SPNs can show better photostability and generate higher PA signal output than two of the best current PA contrast nanoagents, single-wall carbon nanotubes (SWNTs) and gold nanorods (GNRs), on a per mass basis. The high PA brightness in the NIR region and favorable small size of SPNs allowed for PA lymph node (LN) mapping in living mice after a single intravenous administration of low doses (50 μg). By virtue of their facile yet efficient formulation, an SPN-based dual-peak ratiometric PA probe was synthesized for both *in vitro* and *in vivo* imaging of reactive oxygen species (ROS), which are key integral chemical mediators playing vital roles in the onset and progression of pathology ranging from cancer to neurodegenerative and cardiovascular diseases.[27,28] This study thus provides one of the very few examples of NIR activatable PA probes capable of reporting the progression of

pathological processes in real time, and demonstrates the great potential of SPNs for advanced PA imaging in biomedical research.

Results

Synthesis and Characterization

Two photovoltaic SP derivatives with strong absorption in the NIR region, poly(cyclopentadithiophene-*alt*-benzothiadiazole) (SP1)[29] and poly(acenaphthothienopyrazine-*alt*-benzodithiophene) (SP2) (Fig. 1a), were chosen to prepare SPNs. Nanoprecipitation assisted by 1,2-dipalmitoyl-*sn*-glycero-3-phosphocholine (DPPC) (Fig. 1b) afforded water-soluble SP1-based (SPN1) and SP2-based (SPN2) nanoparticles as clear dark-green and olive-green solutions (Fig. 1c), respectively. Transmission electron microscopy (TEM) revealed the spherical morphology of both SPN1 and SPN2, and average diameters of 41±2 and 43±2 nm, respectively (Fig. 1d). Moreover, dynamic light scattering (DLS) confirmed their narrow size distribution with a polydispersity index of 0.16±0.03 for SPN1 and 0.19±0.02 SPN2 (Fig. 1e). SPN1 and SPN2 possessed large zeta potentials of −35±2 and −32±3 mV in PBS (pH = 7.4), respectively, attributable to the presence of DPPC. This excipient resulted in high SPN stability under physiologically relevant conditions (Supplementary Fig. S1).

SPN1 and SPN2 had NIR absorptions with maxima at 660 and 700 nm (Fig. 1f), respectively. Due to the difference in the molecular structures of SP1 and SP2, the peak mass extinction coefficient of SPN1 (93 cm^{-1} mg^{-1} mL) was 4.65-times higher than that of SPN2 (20 cm^{-1} mg^{-1} mL). While SPN1 was fluorescent upon excitation at 680 nm with emission maximum at 838 nm and a quantum yield of 0.1% in 1×PBS at pH = 7.4 (Supplementary Fig. S2), SPN2 did not show detectable FL below 900 nm. With strong absorption in the NIR region, both SPNs efficiently generated PA signals upon NIR pulsed laser irradiation (Fig. 1f). The narrower PA spectral profile of SPN1 was due to narrower absorption above 600 nm relative to SPN2 (Fig. 1f). The maximum PA signals were observed at 690 and 705 nm for SPN1 and SPN2, respectively, both of which were red-shifted as compared to their maximum absorption.

The PA amplitudes of both SPNs at 700 nm were determined at different concentrations in an agar phantom, displaying a linear relationship between PA signal and concentration for SPN1 and SPN2 (Fig. 1g). The narrower PA spectral profile and 5-fold greater PA amplitude of SPN1, attributable to its larger extinction coefficient, as compared with those of SPN2, make SPN1 a better platform for the construction of PA molecular imaging probes.

The capability of SPN1 to produce both FL and PA signals enabled a direct comparison of PA and FL imaging in terms of SPN performance. Two polyethylene (PE) tubes filled with SPN1 were implanted in a tissue-mimicking gelatin phantom (Supplementary Fig. S3), and in the mouse leg (Supplementary Fig. S4). In both examples, PA imaging with SPN1 provided better spatial resolution and much larger penetration depths relative to FL imaging.

Comparison with SWNT and GNR

The PA properties of SPN1 were compared with high-performing PA contrast agents, SWNT and GNR,[14,19] in both agar phantoms and living mice. The SWNT produced strong PA amplitude at 690 nm and the GNR had a PA maximum at 705 nm (Supplementary Fig. S5),[14,19,30] which were spectrally similar to SPN1 (690 nm) and thus permitted direct comparison with a 700 nm pulsed laser. At the same mass concentration, the PA amplitude of SPN1 was 5.2 and 7.1-times higher than SWNT and GNR, respectively (Fig. 2a). Although this result was qualitatively consistent with the rank order of their mass extinction coefficients (93, 50 and 45 cm^{-1} mg^{-1} mL for SPN1, SWNT and GNR, respectively), the large differences in their PA signal amplitude suggested that additional mechanisms, such as the difference in heat conductance and heat capacity, should be relevant. At equal molar concentrations, GNR provided the highest PA amplitude (Fig. 2a) on account of its larger molar mass and molar extinction coefficient (5.0×10^7, 6.0×10^6, and 3.0×10^9 M^{-1} cm^{-1} for SPN1, SWNT and GNR, respectively). However, after exposure to 2.4×10^4 pulses (corresponding to the total laser exposure time of 120 μs) at 9 mJ cm^{-2} fluence, the PA signal of GNR decreased by 30±3% (Fig. 2b), indicating its poor stability from laser-induced deformation.[31] In contrast, no PA signal was lost for SPN1 under the same conditions, revealing its superior photostability and suitability for long-term PA molecular imaging.

The ability to detect nanoparticle PA signal in living subjects was tested through subcutaneous injections of matrigel-containing solutions of SPN1, SWNT or GNR at different concentrations into the dorsal area of mice. Linear correlations between the concentration and the PA signal were observed for all nanoparticles (Fig. 2c). At each concentration, the PA amplitude of SPN1 was ~4.0 and 5.8-times higher than SWNT and GNR, respectively, which were similar to that in agar phantoms. The limit of detection of SPN1 in living mice was ~2 μg/mL (3.8 nM), however neither SWNT nor GNR was detectable at concentrations of 8 μg/mL (Fig. 2d), with PA signals approaching that of tissue background as calculated from the average PA signal in areas free from nanoparticles. This coincides with previous reports that set the limit of detection for SWNT and GNR in living mice by PA tomography close to 9 μg/mL.[13–15]

PA Imaging of Lymph Nodes (LN)

Nanoparticles with diameters ranging from 20 to 50 nm have favorable accumulation and retention in draining LN, and thus are promising for LN tracking, which is clinically important to guide surgical resection of tumor tissues.[32,33] SPN1 (50 μg) were administered intravenously (i.v.) to healthy mice (n = 4) for LN imaging. At 24 h post-injection, the mice were imaged with both PA and FL modalities (Fig. 3a&b). Strong PA and FL signals were detected in the lymphatic networks of living mice, including accumulation in brachial lymph nodes (BLNs), inguinal lymph nodes (ILNs) and superficial cervical lymph nodes (SCLNs), which were undetectable prior to nanoparticle administration (Supplementary Fig. S6). The high accumulation of SPN1 in the LN was confirmed following necropsy, showing that the second highest nanoparticle accumulation occurred in the LN with a fluorescence intensity that is 63% of that from liver (Supplementary Fig. S7). *Ex vivo* LN imaging in an agar phantom showed a 13.3-fold enhancement in PA signal following SPN administration

relative to LN from a mouse receiving saline (Fig. 3c&d), which was similar to the observed FL signal enhancement (12.3-times). This result demonstrates that SPN1 can be used for LN mapping with both PA and FL imaging.

Ratiometric PA Imaging of ROS

The imaging of ROS is critical to understanding the etiology of disease and optimizing therapeutic interventions against potentially life-threatening conditions. SPN1 itself has high stability toward ROS (Supplementary Fig. S8), and thus we coupled it to a cyanine dye derivative (IR775S) that is sensitive to ROS-mediated oxidation (Supplementary Fig. S9) to design a ratiometric PA probe (RSPN) for ROS imaging (Fig. 4a). One-pot nanoprecipitation of IR775S and SP1 with DPPC yielded the water-soluble RSPN (Fig. 4a), which possessed a small diameter (45 nm) and good size stability similar to SPN1 (Supplementary Fig. S10). The average number of IR775S per nanoparticle was estimated to be 50 based on the molar extinction coefficients of SPN1 and IR775S. The PA spectrum of RSPN showed three maxima at 700, 735, and 820 nm (Fig. 4b) with nearly the same amplitude, which differed from its absorption spectrum (Supplementary Fig. S11a): the peak at 700 nm corresponds to the SP1, and the peaks at 735 and 820 nm correspond to IR775S, which has a concentration-dependent PA spectrum. While a single PA peak at 780 nm is observed at low concentrations (0.01–0.04 mg/mL), an additional peak at 820 nm occurs at higher dye concentrations (0.10 mg/mL) (Supplementary Fig. S11b); This is likely due to dye aggregation at elevated concentrations and the photosaturation effect induced by the high-power pulsed laser excitation used for the PA measurements.[30] Accordingly, as the local concentration of IR775S within the compact inner space of the nanoparticle is very high (corresponding to ~2.5 mM), the PA spectrum of RSPN also gave the same two peaks at 735 and 820 nm.

The PA response of RSPN toward different ROS was examined in solution under physiological conditions. In the presence of $ONOO^-$ and ClO^-, the PA peak at 735 nm decreased significantly while that at 820 nm almost disappeared, however the peak at 700 nm remained nearly the same (Fig. 4b). In contrast, in the presence of other ROS such as $^{\bullet}NO$, $^{\bullet}OH$, $O_2^{\bullet-}$, $^1O_2$ and H_2O_2, the PA spectrum remained essentially unchanged (Fig. 4b). The PA spectral change at 820 nm was attributed to the ROS-mediated rapid oxidative decomposition of IR775S (Supplementary Fig. S9),[34] validating the amenability of RSPN to dual-peak ratiometric detection of ROS (PA_{700}/PA_{820}). The enhanced specificity of RSPN toward $ONOO^-$ and ClO^-relative to unencapsulated IR775S likely stems from its nanoencapsulation, which limits interference from other ROS with shorter lifetimes.[35] The PA ratio of RSPN increased from 1.2 to 25 in the presence of $ONOO^-$ and ClO^-, remaining less than 4 for other ROS (Fig. 4C). With a good linear correlation between PA ratio and $ONOO^-/ClO^-$ concentration and a limit of detection of ~50 nM (Supplementary Fig. S12), RSPN showed a large dynamic signal range and high sensitivity to detect both ROS at pathologically relevant concentrations.[28]

The capability of RSPN to detect endogenously generated ROS was then tested incultured murine macrophage RAW264.7 cells. After validating that SPNs have low cytotoxicity and efficient cell uptake (Supplementary Fig. S13), RSPN were incubated with RAW264.7, and

cell pellets were loaded into an agar phantom for PA imaging. For cells in the resting state, a strong PA signal was observed at both 700 and 820 nm (Fig. 4d), resulting in PA_{700}/PA_{820}=1.4±0.43 (Fig. 4e). To mimic the inflammatory condition that stimulates resting macrophages to produce ROS, RAW264.7 cells were pre-treated with bacterial cell wall lipopolysaccharide (LPS) and a dimerized soluble cytokine, interferon-γ (INF-γ). Following LPS/INF-γ stimulation, the PA signal at 820 nm was nearly abolished, (Fig. 4d), leading to an enhanced PA_{700}/PA_{820} of 7.3±0.96 (Fig. 4e). When *N*-acetylcysteine (NAC), a free-radical scavenger with high membrane permeability,[36] was used to treat the cells along with LPS/ INF-γ stimulation, PA_{700}/PA_{820} returned to a low value (3.3±0.78), indicating the scavenging of macrophage-generated ROS by NAC and inhibition of RSPN activation. An overlay of pseudocolored PA images (Fig. 4d), where green and red represent PA signals at 700 and 820 nm, respectively, facilitated the monitoring of ROS levels in cells. The dramatic ratiometric PA responses of RSPN were easily discernible between the resting RAW264.7 cells, the stimulated cells and the NAC-protected cells, with yellow representing a PA ratio near unity and green representing a significant elevation of ROS.

RSPN was applied for the *in vivo* PA imaging of ROS in a murine model of acute edema. Zymosan, a structural polysaccharide of the cell wall of *Saccharomyces cerevisiae*, which, similarly to LPS, can simulate the generation of ROS such as $ONOO^-$ and ClO^- *in vivo*,[37] or saline was injected intramuscularly into the thigh of living mice, followed 20 min later by the injection of RSPN (3 μg in saline) into the same location. The PA signal was simultaneously monitored at 700 and 820 nm, as illustrated by pseudo green and red colors, respectively. The PA amplitude at 700 nm for both saline- and zymosan-treated mice remained nearly unchanged over time (Fig. 5a). The progressive enlargement in signaling area was attributed to tissue diffusion of nanoparticles over time. In contrast, both the PA amplitude and area of signal production at 820 nm for zymosan-treated mice significantly decreased over time (Fig. 5a). The superposition analysis delineated a progressive pseudocolor variation from yellow to green for zymosan-treated mice but not for control mice (Fig. 5a), reporting the *in situ* generation of inflammatory ROS during edema. Quantitative analysis revealed that PA_{700}/PA_{820} gradually increased to 2.7±0.31 at 120 min post-injection for zymosan-treated mice, which was significantly elevated relative to that for control mice (1.4±0.22) (Fig. 5b). Thus, RSPN effectively detected *in vivo* ROS production using a dual-peak ratiometric PA contrast mechanism, demonstrating the potential of SPNs for activatable PA imaging of the progression of pathological processes in real time.

Discussion

Photovoltaic SPs have been made into nanoparticles that produce ultrasound signals upon pulsed NIR laser irradiation. These purely organic PA nanoparticles have a unique set of advantages that derive from their precursor SPs, including a large mass extinction coefficient and high photostability, providing stronger (on a per mass basis) and more photostable PA signals in the NIR region when compared with SWNT and GNR (Fig. 2). At the same mass concentration, the PA amplitude of SPN1 at 700 nm was more than 5-times that of SWNT and GNR (Fig. 2a), effectively reducing their detection limit (2 μg/mL) in living mice relative to both SWNT and GNR (9 μg/mL) (Fig. 2d), which could decrease dosing levels for *in vivo* PA imaging applications. Their favorable size (~40 nm) enabled

efficient PA imaging of major LN in living mice with a high signal-to-noise ratio of 13.3 after a single low dose (50 μg) intravenous administration (Fig. 3). Although detailed toxicity investigations are required for clinical translation, our preliminary studies have shown no overt SPN cytotoxicity (Supplementary Fig. S13a). Others have also reported that the implantation of SPs in living animals invoked little adverse tissue response with no evidence of acute and subacute toxicity.[38] This level of biocompatibility was comparable to the FDA-approved poly(lactic acid-*co*-glycolic acid),[38] suggesting their great promise for clinical applications.

SPNs are readily prepared through a nanoprecipitation-based bottom-up approach, allowing for facile adjustment of PA properties by choosing different constituent photovoltaic SPs without significantly affecting particle dimensions. For example, SPN1 and SPN2 displayed similar sizes (~40 nm) but different PA spectral profiles (Fig. 1d & 1g). This independence of photophysical properties from particle size differentiates SPNs from many of the metallic nanoparticles with strongly size-dependent spectral properties.[18,19] This attribute of SPNs is beneficial to *in vivo* multiplexed imaging, as nanoparticles can be formulated to have distinct PA wavelengths without altering pharmacokinetic profiles. Additionally, other molecules, such as dyes and drugs, may be simultaneously doped into SPNs during nanoprecipitation, potentially endowing properties to SPNs beyond sole PA imaging.

The synthetic and structural flexibility of SPNs permitted the further development of SPN1 into an activatable NIR ratiometric PA probe (RSPN) for *in vivo* ROS imaging. To our knowledge, this study is the first demonstration of a PA imaging probe to detect ROS, since existing ROS probes are mainly based on FL imaging.[39,40] Among nanoparticle agents, SPNs uniquely possess properties of a narrow PA spectral profile, good photostability and a ROS-inert PA signal. Neither SWNT (planar PA spectrum, Supplementary Fig. S5b)[14] nor GNR (poor photostability and poor stability to ROS, Fig 2b & Supplementary Fig. S8a, respectively) possess all of these characteristics necessary for designing ratiometirc ROS probes. Porphysomes are purely organic and photostable PA nanoagents with PA brightness similar to GNRs,[16] however the porphyrin-derived generation of singlet oxygen under laser irradiation limits their application for ROS detection and makes them more well-suited to photo-induced therapy applications. Coupling of the excellent resistance to oxidation of SPN1 with the ROS sensing ability of IR775S, ROS were effectively detected by RSPN with PA ratiometric signal enhancements of 25, 7.3, and 2.7-times in solution (Fig. 4c), in cells (Fig. 4e) and in living mice (Fig. 5b), respectively, comparable to that reported for FL probes.[39,40] As PA imaging has the advantages of deep tissue penetration, high spatial resolution (Supplementary Fig. S3&S4), and the capability to simultaneously acquire anatomical and molecular information, RSPN can further outperform existing FL probes, allowing interrogation of the key role of ROS in the etiology of diseases at levels not achievable by FL imaging.

In summary, we have introduced SPNs as a new class of NIR PA contrast agents for *in vivo* PA molecular imaging. They can serve not only as simple accumulation-based probes (as demonstrated for LN mapping) but also as a nanoplatform to develop activatable probes (as shown by ratiometric PA imaging of ROS in living mice). Given the many key merits of SPNs, we believe that SPNs can provide opportunities for advanced PA molecular imaging,

from facilitating the preclinical investigation of physiological and pathological processes in living subjects to enhancing the PA imaging modality now in the process of clinical translation.

Supplementary Material

Refer to Web version on PubMed Central for supplementary material.

Acknowledgments

We acknowledge the use of the SCi^3 Core Facility. This work was supported by the NIH grants 2R01DK099800-06, R21CA138353A2, the Stanford University National Cancer Institute (NCI) CCNE-T grant (U54CA119367) and ICMIC (P50CA114747). A.J.S. also tanks the Susan G. Komen For The Cure for fellowship support. J.V.J. acknowledges the grant from NCI 5R25CA11868 and was supported by a Postdoctoral Fellowship, PF-13-098-01–CCE from the American Cancer Society.

References

1. Mei J, Diao Y, Appleton AL, Fang L, Bao Z. Integrated materials design of organic semiconductors for field-effect transistors. J Am Chem Soc. 2013; 135:6724–6746. [PubMed: 23557391]
2. Peet J, et al. Efficiency enhancement in low-bandgap polymer solar cells by processing with alkane dithiols. Nat Mater. 2007; 6:497–500. [PubMed: 17529968]
3. Sokolov AN, Tee BCK, Bettinger CJ, Tok JBH, Bao ZN. Chemical and Engineering Approaches To Enable Organic Field-Effect Transistors for Electronic Skin Applications. Accounts Chem Res. 2012; 45:361–371.
4. Rose A, Zhu Z, Madigan CF, Swager TM, Bulovic V. Sensitivity gains in chemosensing by lasing action in organic polymers. Nature. 2005; 434:876–879. [PubMed: 15829959]
5. Sanghvi AB, Miller KP, Belcher AM, Schmidt CE. Biomaterials functionalization using a novel peptide that selectively binds to a conducting polymer. Nat Mater. 2005; 4:496–502. [PubMed: 15895095]
6. Wu C, Chiu DT. Highly fluorescent semiconducting polymer dots for biology and medicine. Angew Chem Int Ed Engl. 2013; 52:3086–3109. [PubMed: 23307291]
7. Zhu C, Liu L, Yang Q, Lv F, Wang S. Water-soluble conjugated polymers for imaging, diagnosis, and therapy. Chem Rev. 2012; 112:4687–4735. [PubMed: 22670807]
8. Xiong L, Shuhendler AJ, Rao J. Self-luminescing BRET-FRET near-infrared dots for in vivo lymph-node mapping and tumour imaging. Nat Commun. 2012; 3:1193. [PubMed: 23149738]
9. Pu KY, Liu B. Fluorescent Conjugated Polyelectrolytes for Bioimaging. Advanced Functional Materials. 2011; 21:3408–3423.
10. Wang LV, Hu S. Photoacoustic tomography: in vivo imaging from organelles to organs. Science. 2012; 335:1458–1462. [PubMed: 22442475]
11. Ntziachristos V, Razansky D. Molecular imaging by means of multispectral optoacoustic tomography (MSOT). Chem Rev. 2010; 110:2783–2794. [PubMed: 20387910]
12. Kim C, Favazza C, Wang LHV. In Vivo Photoacoustic Tomography of Chemicals: High-Resolution Functional and Molecular Optical Imaging at New Depths. Chem Rev. 2010; 110:2756–2782. [PubMed: 20210338]
13. Eghtedari M, et al. High sensitivity of in vivo detection of gold nanorods using a laser optoacoustic imaging system. Nano Letters. 2007; 7:1914–1918. [PubMed: 17570730]
14. De la Zerda A, et al. Carbon nanotubes as photoacoustic molecular imaging agents in living mice. Nat Nanotechnol. 2008; 3:557–562. [PubMed: 18772918]
15. Kim JW, Galanzha EI, Shashkov EV, Moon HM, Zharov VP. Golden carbon nanotubes as multimodal photoacoustic and photothermal high-contrast molecular agents. Nature Nanotechnology. 2009; 4:688–694.

16. Lovell JF, et al. Porphysome nanovesicles generated by porphyrin bilayers for use as multimodal biophotonic contrast agents. Nature Materials. 2011; 10:324–332. [PubMed: 21423187]
17. Akers WJ, et al. Noninvasive Photoacoustic and Fluorescence Sentinel Lymph Node Identification using Dye-Loaded Perfluorocarbon Nanoparticles. ACS Nano. 2011; 5:173–182. [PubMed: 21171567]
18. Xia YN, et al. Gold Nanocages: From Synthesis to Theranostic Applications. Accounts Chem Res. 2011; 44:914–924.
19. Jokerst JV, Cole AJ, Van de Sompel D, Gambhir SS. Gold Nanorods for Ovarian Cancer Detection with Photoacoustic Imaging and Resection Guidance via Raman Imaging in Living Mice. ACS Nano. 2012; 6:10366–10377. [PubMed: 23101432]
20. Lovell JF, Liu TW, Chen J, Zheng G. Activatable photosensitizers for imaging and therapy. Chem Rev. 2010; 110:2839–2857. [PubMed: 20104890]
21. Razgulin A, Ma N, Rao JH. Strategies for in vivo imaging of enzyme activity: an overview and recent advances. Chem Soc Rev. 2011; 40:4186–4216. [PubMed: 21552609]
22. Weissleder R, Ntziachristos V. Shedding light onto live molecular targets. Nat Med. 2003; 9:123–128. [PubMed: 12514725]
23. Melancon MP, Zhou M, Li C. Cancer theranostics with near-infrared light-activatable multimodal nanoparticles. Acc Chem Res. 2011; 44:947–956. [PubMed: 21848277]
24. Levi J, et al. Molecular photoacoustic imaging of follicular thyroid carcinoma. Clin Cancer Res. 2013; 19:1494–1502. [PubMed: 23349314]
25. Levi J, et al. Design, Synthesis, and Imaging of an Activatable Photoacoustic Probe. Journal of the American Chemical Society. 2010; 132:11264–11269. [PubMed: 20698693]
26. Zhang Y, Hong H, Cai W. Photoacoustic imaging. Cold Spring Harbor protocols. 201110.1101/pdb.top065508
27. Medzhitov R. Origin and physiological roles of inflammation. Nature. 2008; 454:428–435. [PubMed: 18650913]
28. Szabo C, Ischiropoulos H, Radi R. Peroxynitrite: biochemistry, pathophysiology and development of therapeutics. Nat Rev Drug Discov. 2007; 6:662–680. [PubMed: 17667957]
29. Muhlbacher D, et al. High photovoltaic performance of a low-bandgap polymer. Advanced Materials. 2006; 18:2884–2889.
30. Pramanik M, Swierczewska M, Green D, Sitharaman B, Wang LV. Single-walled carbon nanotubes as a multimodal-thermoacoustic and photoacoustic-contrast agent. J Biomed Opt. 2009; 14
31. Link S, Burda C, Nikoobakht B, El-Sayed MA. Laser-induced shape changes of colloidal gold nanorods using femtosecond and nanosecond laser pulses. Journal of Physical Chemistry B. 2000; 104:6152–6163.
32. Kim S, et al. Near-infrared fluorescent type II quantum dots for sentinel lymph node mapping. Nat Biotechnol. 2004; 22:93–97. [PubMed: 14661026]
33. Nakajima M, Takeda M, Kobayashi M, Suzuki S, Ohuchi N. Nano-sized fluorescent particles as new tracers for sentinel node detection: Experimental model for decision of appropriate size and wavelength. Cancer Sci. 2005; 96:353–356. [PubMed: 15958058]
34. Oushiki D, et al. Development and Application of a Near-Infrared Fluorescence Probe for Oxidative Stress Based on Differential Reactivity of Linked Cyanine Dyes. Journal of the American Chemical Society. 2010; 132:2795–2801. [PubMed: 20136129]
35. Kim G, Lee YE, Xu H, Philbert MA, Kopelman R. Nanoencapsulation method for high selectivity sensing of hydrogen peroxide inside live cells. Anal Chem. 2010; 82:2165–2169. [PubMed: 20163178]
36. Winterbourn CC, Metodiewa D. Reactivity of biologically important thiol compounds with superoxide and hydrogen peroxide. Free Radic Biol Med. 1999; 27:322–328. [PubMed: 10468205]
37. Zhao G, et al. Pivotal role of reactive oxygen species in differential regulation of lipopolysaccharide-induced prostaglandins production in macrophages. Mol Pharmacol. 2013; 83:167–178. [PubMed: 23071105]

38. Guimard NK, Gomez N, Schmidt CE. Conducting polymers in biomedical engineering. Prog Polym Sci. 2007; 32:876–921.
39. Dickinson BC, Chang CJ. Chemistry and biology of reactive oxygen species in signaling or stress responses. Nat Chem Biol. 2011; 7:504–511. [PubMed: 21769097]
40. Nagano T. Bioimaging probes for reactive oxygen species and reactive nitrogen species. J Clin Biochem Nutr. 2009; 45:111–124. [PubMed: 19794917]

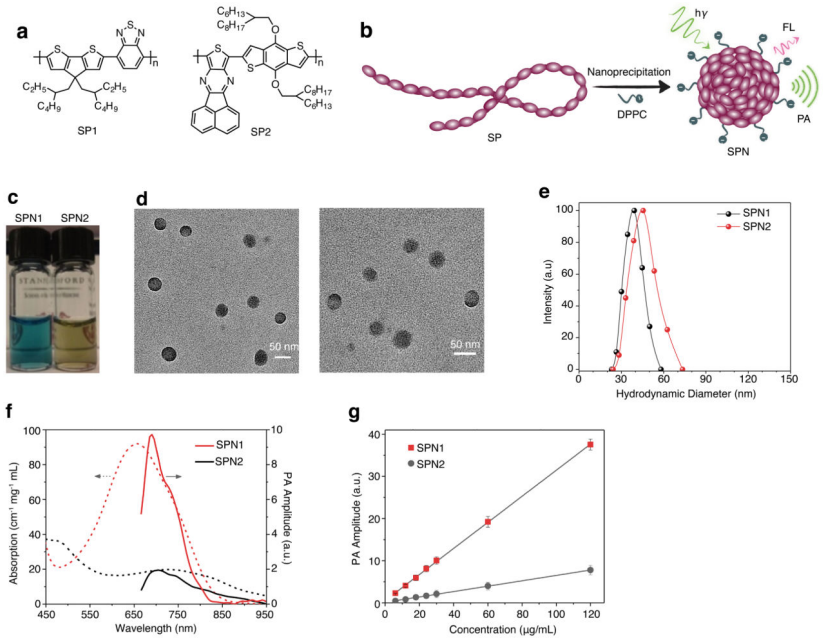

Figure 1. Synthesis and characterization of SPNs

(**a**) Molecular structures of SP1 and SP2 used for the preparation of SPN1 and SPN2, respectively. (**b**) Schematic of the preparation of SPNs through nanoprecipitation. SP is represented as a long chain of chromophore units illustrated as red oval beads. DPPC contains a short hydrophobic tail and a charged head, and is illustrated as a string with a dark green ball at its end. (**c**) Photographic images of the SPN solutions (10 μg/mL). (**d**) Representative TEM images of SPN1 (left) and SPN2 (right). (**e**) Representative DLS profiles of SPNs. (**f**) UV-Vis absorption (dash lines) and PA spectra (solid lines) of SPNs. (**g**) PA amplitudes of SPNs at 700 nm in an agar phantom as a function of mass concentration. R^2 = 0.998 and 0.997 for SPN1 and SPN2, respectively. Error bars represent standard deviation of three separate measurements.

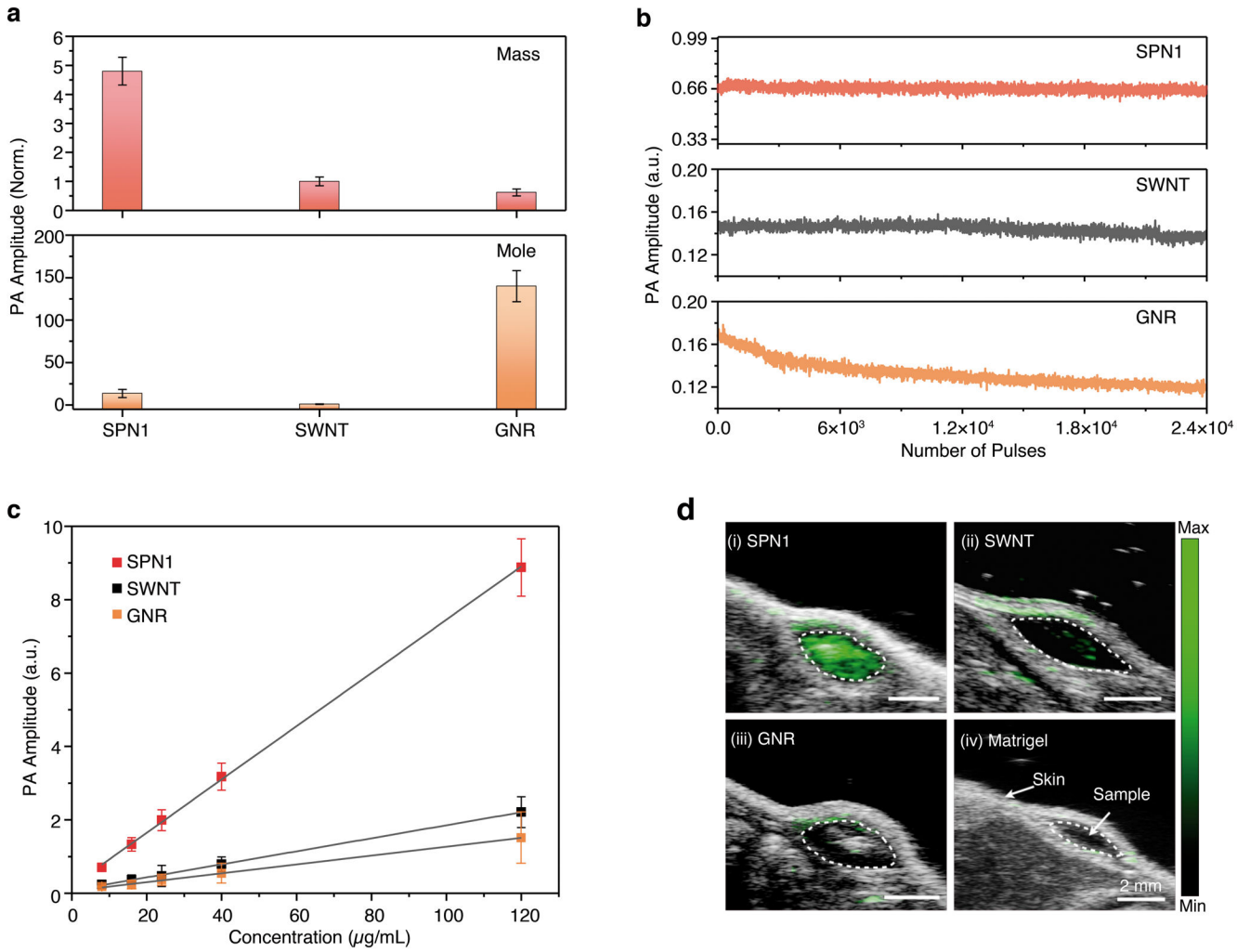

Figure 2. Comparison of PA properties of SPN1 with SWNT (1.2 × 150 nm) and GNR (15 × 40 nm)

(**a**) PA amplitudes of the nanoparticles based on the same mass (25 μg/mL) (top) and molar (48 nM) (bottom) concentrations in an agar phantom. (**b**) PA amplitudes of indicated nanoparticles in agar phantoms versus number of laser pulses; the total laser exposure time was 120 μs for 24,000 pulses. (**c**) PA amplitudes of the nanoparticle-matrigel inclusions (30 μL) in the subcutaneous dorsal space of living mice as a function of nanoparticle mass concentration. The tissue background signal calculated as the average PA signal in areas where no nanoparticles were injected was 0.21 ± 0.03 a.u. R^2 = 0.992, 0.990 and 0.992 for SPN1, SWNT, and GNR, respectively. (**d**) PA/US coregistered images of the nanoparticle-matrigel inclusions at a concentration of 8 μg/mL. The images represent transverse slices through the subcutaneous inclusions (dotted circles). A single laser pulse at 700 nm with a laser fluence of 9 mJ cm^{-2} and a pulse repetition rate of 20 Hz were used for all experiments. All data represent standard deviation of three separate measurements.

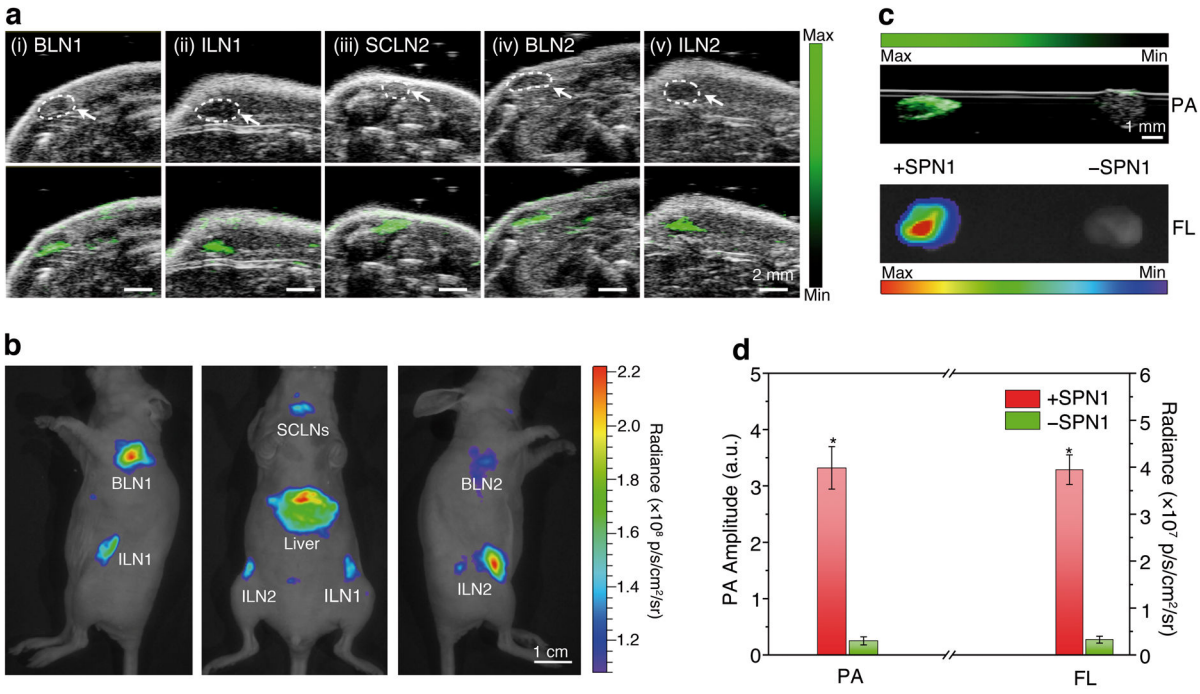

Figure 3. *In vivo* and *ex vivo* PA and FL imaging of lymph nodes using SPN1

(**a**) US (upper) and PA/US coregistered (lower) images of mouse lymph nodes following tail vain injection of SPN1 (50 μg/mouse). The images represent transverse slices through the lymph nodes. BLN: brachial lymph node; ILN: inguinal lymph node; SCLN: superficial cervical lymph node. (**b**) FL/bright-field images of the corresponding mouse. (**c**) *Ex vivo* PA/US coregistered (top) and FL/bright-field (bottom) images of resected lymph nodes from the mouse in (**a**) (left) or a control mouse without SPN1 injection (right) in an agar phantom. (**d**) *Ex vivo* quantification of PA and FL signals of the lymph nodes from SPN1-administrated mice (n=4) and control mice (n=4). *Statistically significant difference in both PA and FL signals between the lymph nodes from SPN1-administrated and control mice ($p < 0.05$).

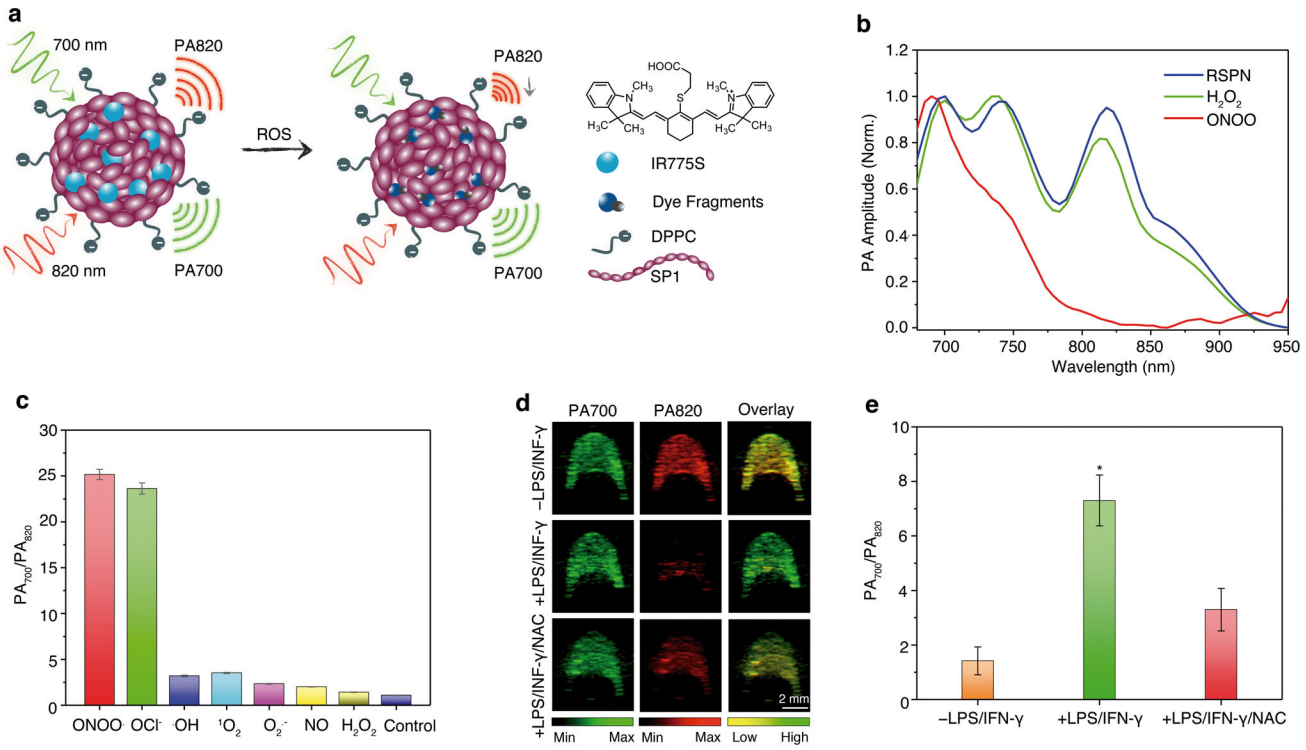

Figure 4. ***In vitro*** **characterization of RSPN for ROS sensing**

(**a**) Proposed ROS sensing mechanism. (**b**) Representative PA spectra of RSPN in the absence and presence of ROS. [RSPN] = 5 μg/mL, [ROS] = 5 μM. (**c**) The ratio of PA amplitude at 700 nm to that at 820 nm (PA_{700}/PA_{820}) after treatment with indicated ROS (5 μM). (**d**) PA images of macrophage RAW264.7 cell pellets (1.5×10^6 cells) without (upper) or with (middle) stimulation with LPS/INF-γ, and with NAC protection (lower). Cell pellets were inserted into an agar phantom and imaged with pulsed laser tuned to (i) 700 nm or (ii) 820 nm, (iii) overlays of images from columns i and ii. The cells were incubated with RSPN (6 μg/mL) for 3 h before trypsinization. (**e**) Quantification of the absorption ratio (PA_{700}/PA_{820}) for macrophage cell pellets with and without LPS/INF-γor LPS/INF-γ/NAC treatment. The error bars represent the standard deviation from four separate measurements. *Statistically significant difference in PA_{700}/PA_{820} between LPS/INF-γ treated and untreated or NAC-protected cell pellets ($p < 0.05$).

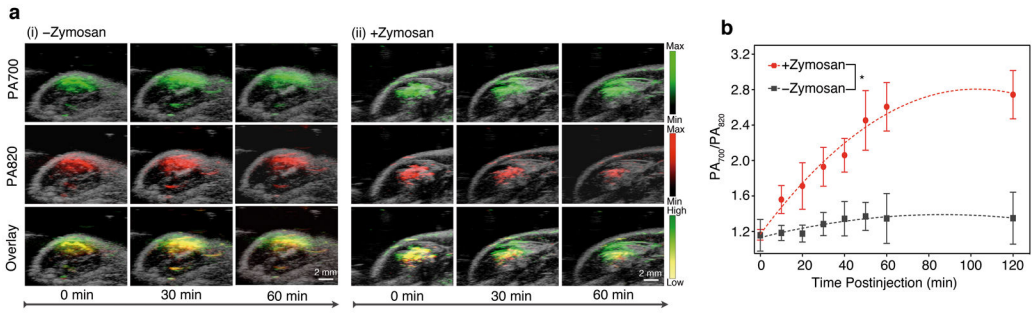

Figure 5. ***In vivo*** **PA imaging of ROS generation from a mouse model of acute edema using RSPN (n=3 each)**

(**a**) PA/US overlaid images of saline-treated (i) and zymosan-treated (ii) regions in the thigh of living mice (n=3). RSPN (3 μg in 50 μL) was intramuscularly injected into the thigh 20 min after zymosan treatment. (**b**) The ratio of PA amplitude at 700 nm to that at 820 nm (PA_{700}/PA_{820}) as a function of time post-injection of RSPN. *Statistically significant difference in PA_{700}/PA_{820} between zymosan-treated and saline-treated mice at all time points starting from 10 min ($p<0.05$).